CORONAL HEATING IN ACTIVE REGIONS AS A FUNCTION OF GLOBAL MAGNETIC VARIABLES

GEORGE H. FISHER

Space Sciences Laboratory, University of California, Berkeley, CA 94720-7450; fisher@ssl.berkeley.edu

DANA W. LONGCOPE[1]

Physics Department, Montana State University, Bozeman, MT 59717-3840; dana@physics.montana.edu

THOMAS R. METCALF

Lockheed Martin Advanced Technology Center, Department H1-12 B252, 3251 Hanover Street, Palo Alto, CA 94304; metcalf@lmsal.com

AND

ALEXEI A. PEVTSOV

Physics Department, Montana State University, Bozeman, MT 59717-3840; pevtsov@physics.montana.edu

Received 1998 March 27; accepted 1998 July 7

ABSTRACT

A comparison of X-ray images of the Sun and full disk magnetograms shows a correlation between the locations of the brightest X-ray emission and the locations of bipolar magnetic active regions. This correspondence has led to the generally accepted idea that magnetic fields play an essential role in heating the solar corona.

To quantify the relationship between magnetic fields and coronal heating, the X-ray luminosity of many different active regions is compared with several global (integrated over entire active region) magnetic quantities. The X-ray measurements were made with the SXT Telescope on the *Yohkoh* spacecraft; magnetic measurements were made with the Haleakala Stokes Polarimeter at the University of Hawaii's Mees Solar Observatory.

The combined data set consists of 333 vector magnetograms of active regions taken between 1991 and 1995; X-ray luminosities are derived from time averages of SXT full-frame desaturated (SFD) images of the given active region taken within ± 4 hours of each magnetogram. Global magnetic quantities include the total unsigned magnetic flux $\Phi_{tot} \equiv \int dA \, |B_z|$, $B_{z,tot}^2 \equiv \int dA B_z^2$, $J_{tot} \equiv \int dA \, |J_z|$, and $B_{\perp,tot}^2 \equiv \int dA B_\perp^2$, where J_z is the vertical current density and B_z and $B_\perp$ are the vertical and horizontal magnetic field amplitudes, respectively.

The X-ray luminosity L_X is highly correlated with all of the global magnetic variables, but it is best correlated with the total unsigned magnetic flux Φ_{tot}. The correlation observed between L_X and the other global magnetic variables can be explained entirely by the observed relationship between those variables and Φ_{tot}. In particular, no evidence is found that coronal heating is affected by the current variable J_{tot} once the observed relationship between L_X and Φ_{tot} is accounted for. A fit between L_X and Φ_{tot} yields the relationship $L_X \simeq 1.2 \times 10^{26}$ ergs s$^{-1} (\Phi_{tot}/10^{22}$ Mx$)^{1.19}$.

The observed X-ray luminosities are compared with the behavior predicted by several different coronal heating theories. The Alfvén wave heating model predicts a best relationship between L_X and Φ_{tot}, similar to what is found, but the observed relationship implies a heating rate greater than the model can accommodate. The "Nanoflare Model" of Parker predicts a best relationship between L_X and $B_{z,tot}^2$ rather than Φ_{tot}, but the level of heating predicted by the model can still be compared to the observed data. The result is that for a widely used choice of the model parameters, the nanoflare model predicts 1.5 orders of magnitude more heating than is observed. The "Minimum Current Corona" model of Longcope predicts a qualitative variation of L_X with Φ_{tot} that agrees with what is observed, but the model makes no quantitative prediction that can be tested with the data. A comparison between L_X and the magnetic energy E_{mag} in each active region leads to a timescale that is typically 1 month, or about the lifetime of an active region, placing an important observational constraint on coronal heating models.

Comparing the behavior of solar active regions with nearby active stars suggests that the relationship observed between L_X and Φ_{tot} may be a fundamental one that applies over a much wider range of conditions than is seen on the Sun.

Subject headings: Sun: activity — Sun: corona — Sun: magnetic fields — Sun: X-rays, gamma rays

1. INTRODUCTION

The physical mechanism(s) responsible for heating the solar corona to temperatures in excess of 10^6 K has been a puzzle since the 6374 Å "coronium" line observed during eclipses was first identified as a line of highly ionized iron (Fe x; Grotrian 1939; Edlen 1937). High-resolution images of the corona in the extreme ultraviolet and X-ray wave-

length bands are now routinely made with the EIT telescope on *SOHO* (Delaboudiniere et al. 1995) and the Soft X-Ray Telescope (SXT) on *Yohkoh* (Tsuneta et al. 1991). These spectacular observations have revealed many details of the coronal structure and evolution, but the underlying processes that heat it remain poorly understood. X-ray and EUV images show bright coronal loops that resemble coronal magnetic field lines, suggesting an intimate connection between the magnetic field and heating mechanisms.

The connection between magnetic fields and coronal

---

[1] Also, Space Sciences Laboratory, University of California, Berkeley, CA 94720-7450.

heating is especially compelling when the contributions of the different parts of the Sun's corona to the total X-ray luminosity are examined in detail. Roughly half of the Sun's X-ray luminosity comes from a tiny fraction ($\sim 2\%$) of the solar disk (Acton 1996). Virtually all of the Sun's X-ray luminosity is concentrated within active regions, where the Sun's magnetic field is strongest. While the corona is evidently heated everywhere, there is no question that it is heated most intensely within active regions and that active regions contribute essentially all of the X-rays that would be seen if the Sun were observed as a star (i.e., spatially unresolved). For these reasons, this paper will focus entirely on active regions.

The energy that heats the corona almost certainly propagates upward across the photosphere. If the magnetic field plays a dominant role, the required energy flux can be expressed in terms of the electromagnetic Poynting flux

$$S_z = \frac{c}{4\pi} (E \times B)_z = -\frac{1}{4\pi} (v \cdot B) B_z \,, \qquad (1)$$

where we have assumed that the vertical plasma velocity v_z vanishes. In a frequently cited survey of *Skylab* X-ray data (Withbroe & Noyes 1977) a value of $S_z \sim 10^7$ ergs cm^{-2} s^{-1} is found necessary to account for the X-ray flux from active regions.

Detailed heating models typically invoke mechanisms belonging to one of the two broadly defined categories of wave (AC) or stress (DC) heating. In wave heating, the large-scale magnetic field acts essentially as a conduit for small-scale, high-frequency Alfvén waves propagating into the corona. Assuming perfect absorption in the corona, the average flux of wave energy is

$$\langle S_z \rangle = \sqrt{\frac{\rho}{4\pi}} \langle v^2 \rangle B_z \,, \qquad (2)$$

where the B_z is the large-scale, stationary magnetic field, ρ is the mass density, and $\langle v^2 \rangle$ is the mean square velocity amplitude of the Alfvén waves.

In stress heating, the coronal magnetic field stores energy in the form of DC electric currents until it can be dissipated through, e.g., nanoflares (Parker 1988). Estimating the rate of energy storage results in a Poynting flux of the form

$$S_z \sim |v| B_z^2 \,, \qquad (3)$$

where the constant of proportionality describes the efficiency of magnetic dissipation, which might involve the random footpoint velocity v (Parker 1983) or simply the geometry (Browning, Sakurai, & Priest 1986; Longcope & Sudan 1994).

One line of investigation of heating mechanisms is to seek *direct* observational evidence of some proposed form of heating. For wave heating models, for example, this involves seeking signatures of Alfvén waves such as non-thermal broadening of transition region spectral lines, or perhaps evidence for a global magnetic resonance from time series analyses of the brightness of individual coronal loops (McKenzie & Mullan 1997). Nonthermal broadening measurements of transition region lines (Cheng, Doschek, & Feldman 1979; Dere & Mason 1993; Warren et al. 1997) routinely result in velocities ~ 20–30 km s^{-1}, consistent with equation (2) and $S_z \sim 10^7$ ergs cm^{-2}s^{-1} (Withbroe & Noyes 1977). To investigate stress heating models, one approach is to estimate the average energy dissipation from

observed microflaring (Hudson 1991), which yields values an order of magnitude lower than that inferred. Another approach is to test the correspondence between regions of enhanced coronal heating, as indicated by, e.g., soft X-ray luminosity and regions where the stored (nonpotential) magnetic energy is large. This approach was pursued for the case of the active region NOAA 6952 (Metcalf et al. 1994), with no correspondence found between X-ray emission and regions of large vertical photospheric current. In contrast, a study of heating within five active regions (Falconer et al. 1997; Moore et al. 1996) did yield a correlation between the brightest X-ray emission and the most strongly sheared magnetic field.

While these direct investigations can determine the presence of an alleged heating agent, they cannot establish that it is responsible for the heating. Furthermore, interpretation of such data requires an understanding of how electromechanical energy, in the form of Alfvén waves or as stressed magnetic fields, is converted to heat. While theoretical solutions to this problem for AC and DC heating are Alfvén wave resonances (Hollweg 1984) and current sheet formation (Parker 1972), respectively, the corresponding uncertainties at this level of the theory can weaken the conclusions of direct investigations. For example, the low efficiency of Alfvén wave damping ($Q \geq 10$; McKenzie & Mullan 1997) should lead to plasma velocities well in excess of those in equation (2) if the estimate for S_z (Withbroe & Noyes 1977) is used. Such large velocities are not observed, leading one to suspect either an alternative heating mechanism (e.g., DC heating) or a dissipation mechanism much more efficient than those yet considered. Conversely, the lack of correspondence between X-ray emission and observed large-scale currents (Metcalf et al. 1994) is consistent with DC heating if current sheet locations do not necessarily coincide with the large-scale currents that can be measured with a vector magnetograph.

We therefore propose an alternative to the direct approach, namely an examination of the statistical correlation between coronal heating and magnetic quantities in a large and diverse sample of observed active regions. The form of such correlations can be used to distinguish between various proposed models of heating. For example, the Poynting flux in equations (2) and (3) scales differently with the magnetic field B_z. While the constants of proportionality in each case may vary due to numerous other factors, we might expect a large enough sample to be capable of distinguishing between the two mechanisms. In addition, one might expect DC heating mechanisms to exhibit a statistical correlation between heating rate and some signature of stress, such as large-scale currents determined from vector magnetograph measurements. The statistical nature distinguishes this approach from the direct studies (Metcalf et al. 1994; Falconer et al. 1997; and Moore et al. 1996) that sought detailed spatial correlations for a single active region or for a small number of active regions. Here we look at active regions as a whole. Statistical studies of coronal heating have been undertaken in the past. *Skylab* soft X-ray data was used in conjunction with Kitt Peak line-of-sight magnetograms (Golub et al. 1980) to establish a relation of the form $U_t \sim \Phi_{tot}^{1.5}$ between the net unsigned flux in an active region Φ_{tot} and its thermal energy content U_t. However, this relation may simply reflect the variation between the surface area and volume of active regions. In another study, the total X-ray luminosity L_X has been

inferred to scale with the total unsigned flux as $L_X \sim \Phi_{tot}^{0.9}$ for statistical samples of late-type stars (Schrijver et al. 1989). Statistical studies have also been performed for individual coronal loops (Porter & Klimchuk 1995; Kano & Tsuneta 1995).

The work described in this paper carries out a statistical investigation of coronal heating using soft X-ray telescope (SXT) images from *Yohkoh* in conjunction with vector magnetograms from the Haleakala Stokes Polarimeter (HSP) at the University of Hawaii's Mees Solar Observatory (MSO) (Mickey 1985). Using 333 vector magnetograms, we define a number of global magnetic quantities that are calculated for each active region measurement. The SXT images are then used to estimate the X-ray luminosity L_X for the active region. The measurements of the global magnetic quantities and L_X are described in § 2. Section 3 explores the relationships of global magnetic quantities with L_X and also with each other. We conclude that the fundamental relationship is between the X-ray luminosity and unsigned magnetic flux: $L_X \sim \Phi_{tot}^{1.19}$. In § 4 we discuss and interpret our results within the context of several coronal heating theories, and in § 5 we present our conclusions and comment on a comparison between heating in solar active regions with that in other active stars.

2. THE DATA SET

2.1. *HSP Vector Magnetograms*

The HSP (Mickey 1985) provides a multiyear vector-magnetogram database that overlaps with the *Yohkoh* mission. The HSP is fed by a telescope of 15 cm aperture; the instantaneous field of view is a circular region 6″ in diameter. The telescope is then raster scanned to gather data for a vector magnetogram. At each point in the scan, full Stokes spectra are recorded. A fiber-fed echelle spectrometer provides high wavelength resolution. The detectors are linear arrays, which simultaneously record 128 spectral points over a range of a few angstroms. The magnetic field parameters are derived from Stokes profiles of the spectral lines Fe I $\lambda\lambda6301.5$ and 6302.5, using a nonlinear least-squares Unno-profile fitting routine (Skumanich & Lites 1987). Analyzing the full Stokes spectra in this way allows one to compensate for saturation effects (which underestimate the amplitude of strong fields), magneto-optic effects (primarily Faraday rotation, which changes the apparent direction of the magnetic field vector), and filling-factor effects (which distort the relationship between longitudinal and transverse magnetic field strengths).

After the longitudinal and transverse magnetic fields have been computed from the polarization measurements, the effects of image foreshortening away from disk center are corrected for, the 180° ambiguity is removed (Canfield et al. 1993; Metcalf 1994), and the magnetic field vectors are expressed in terms of vertical and horizontal components rather than longitudinal and transverse components. Large-scale vertical current densities can then be computed from the horizontal components of the field by taking the curl; care must be taken to not overinterpret these "large-scale" derived currents in terms of the actual distribution of electric currents at the photosphere (Parker 1996).

Errors in determining the ambiguity-resolved vector magnetic field and electric current with the HSP occur primarily from errors in the transverse field. Errors in the transverse field strength at each pixel are typically 150 G;

errors in the computed currents are typically 3 mA m^{-2}. Single-pixel errors in the line of sight component of the magnetic field, on the other hand, are typically 50 G. A discussion of random and systematic errors in determining magnetic fields from polarization measurements can be found in Klimchuk, Canfield, & Rhoads (1992) and Klimchuk & Canfield (1994).

In all cases the HSP data were scanned using a 6″ pinhole. However, the data scans are of two types. In the first type, termed "critically sampled," the pinhole was stepped by 2″.8. In the second, termed "undersampled," the pinhole was stepped by 5″.6. While the undersampled data have degraded spatial resolution, the integration time at each raster point was longer, so the field measurement at each pixel is more accurate than that from the critically sampled data.

One to two hours are required to build up a magnetogram of a typical active region; 1–3 magnetograms are typically taken each day. The typical minimum timescale for significant changes to the magnetic field pattern in an active region is several hours (e.g., Fig. 3 of Metcalf et al. 1994; Pevtsov, Canfield, & Metcalf 1994).

2.2. *Global Magnetic Quantities*

Our strategy is to compute global properties of each active region in our data set from the vector magnetograms, rather than trying to study or explain the evolution of detailed features within active regions. We have used the magnetograms described above to compute the following integrated (global) quantities:

$$\Phi_{tot} \equiv \int dA\, |B_z| \, , \tag{4}$$

$$B_{z,tot}^2 \equiv \int dA\, B_z^2 \, , \tag{5}$$

$$J_{tot} \equiv \int dA\, |J_z| \, , \tag{6}$$

$$B_{\perp,tot}^2 \equiv \int dA\, B_\perp^2 \, . \tag{7}$$

Here $\int dA$ means summation over the area on the solar surface corresponding to the magnetogram, B_z is the vertical component of the magnetic field, $B_\perp$ is the horizontal field amplitude, and J_z is the vertical current density derived by taking the curl of the horizontal components of the field. Only magnetic variables that are 2 σ above the estimated single pixel noise level are included in the integration. We have also computed the "best" value of α_{ls} (the ratio $\mu_0 J_z/B_z$) by doing a least-squares fit of a constant α field to the magnetogram (Pevtsov, Canfield, & Metcalf 1995). We introduce two auxiliary quantities that are related to two of the variables described above:

$$\bar{B} \equiv B_{z,tot}^2/\Phi_{tot} \, , \tag{8}$$

$$\bar{A} \equiv \Phi_{tot}^2/B_{z,tot}^2 \, . \tag{9}$$

$\bar{B}$ and $\bar{A}$ are weighted values of the field strength in the active region and its area, respectively.

An advantage of using integrated quantities is that the relative error is reduced significantly by combining measurements from the many pixels in each magnetogram. The single-pixel errors in the magnetic field measurements are used to estimate the corresponding errors in the global

magnetic variables. Average estimated errors of the global magnetic variables Φ_{tot}, J_{tot}, $B^2_{z,tot}$, and $B^2_{\perp,tot}$ over the entire data set are 4%, 13%, 2%, and 23%, respectively, with relative errors decreasing with the size of the active region. The presence of noise in each pixel also introduces a bias in the quantities $B^2_{z,tot}$ and $B^2_{\perp,tot}$. We estimate this bias as the sum over all pixels used of the square of the error per pixel times the area per pixel. The bias is then subtracted from the global variable.

2.3. Selection of Magnetograms

The magnetograms selected for our study are a subset of the magnetograms that have already been reduced for other studies (Pevtsov et al. 1995). This data set includes observations taken at many different times during the 1991–1995 time frame, includes both small and large active regions, and includes active regions at many locations on the solar disk. Many of the observations are of the same active region, observed repeatedly for periods of several days. For this study, we have excluded magnetograms with a central meridional distance greater than 50° from disk center, and we have also excluded magnetograms falling within 4 hours

of the beginning or end of a *Yohkoh* week boundary. This restriction was made to avoid having to use data from two different *Yohkoh* data tapes in the analysis of a single magnetogram (see § 2.4).

2.4. Coordinated Yohkoh SXT Data

For each selected vector magnetogram, we identify the SXT full disk data taken within ±4 hours of the magnetogram. This 8 hour time window was chosen to be the minimum time over which significant changes might occur in the magnetic field (Metcalf et al. 1994; Pevtsov et al. 1994). From the SXT data within this window, we only use SFD images taken in the thin aluminum filter. The SFD images are created by combining images from short and long exposures and are then normalized to a constant effective 1 s exposure time. The SFD images have the advantage of providing a better dynamic range of X-ray luminosities than would be obtained from single-exposure images.

Each SFD image is "chopped" to a rectangle just large enough to enclose the magnetogram (see Fig. 1). All the chopped SFD images from the selected time window are then averaged together to form a single averaged X-ray
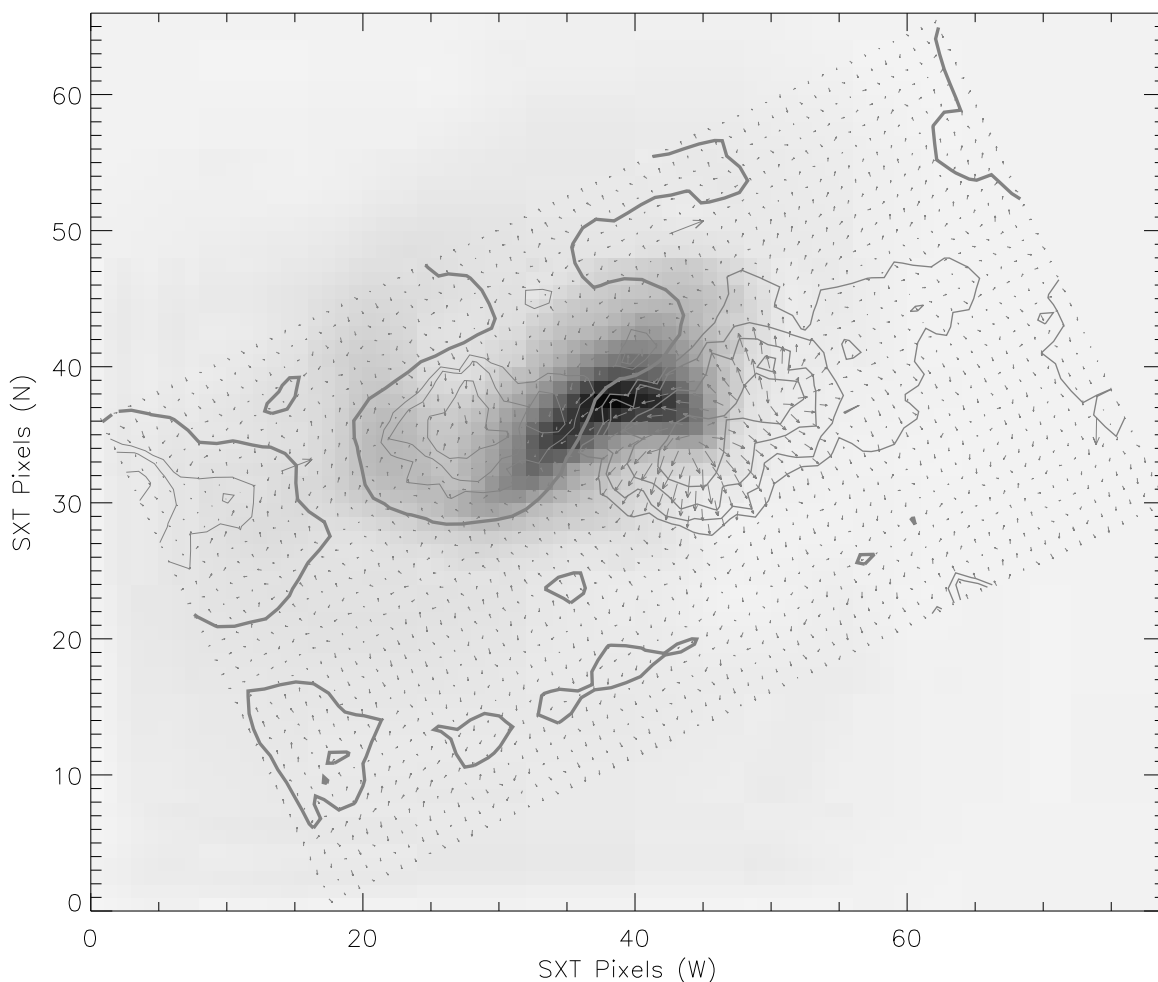

FIG. 1.—Example of the combined SFD and magnetogram data. Shown in gray scale is an overlay of the averaged SFD image in the thin aluminum filter, with the HSP vector magnetogram for active region NOAA 7452 scanned on 1993 March 21 starting at 20:47 UT. Note that the magnetogram is tilted by a P angle of −25°.5 with respect to the X-ray image. The thickest contour line is the smoothed magnetic neutral line. Contours of medium thickness represent upward vertical magnetic field strength at levels of 100, 200, 400, and 800 G, respectively. The thinnest contours represent downward vertical field strength at the same levels. The X-ray emission (the dark region) is concentrated near the magnetic neutral line. Arrows show strength and direction of the horizontal magnetic field. Solar north is up, and solar west is toward the right. Units along axes are in SXT full resolution pixels (2″.455).

image. This is intended to smooth over any rapid variations in the X-ray luminosity.

The averaged image was visually inspected and rejected if, for example, the chopping had cropped out any significant X-ray emission. Of 580 magnetogram/SFD pairs examined, 247 were rejected principally because of this cropping. This reflects a systematic error in the recorded magnetogram position, which placed it north and west of its true position on the solar disk. This left a total of 333 magnetogram/SFD pairs that make up our data set.

The averaged, chopped SFD image, once accepted, was then used to determine an averaged X-ray luminosity L_X in ergs s^{-1}. The SFD count rates (DN s^{-1}) were converted to ergs s^{-1} emitted between 1 and 300 Å using standard *Yohkoh* SXT software, assuming a coronal temperature $T = 3 \times 10^6$ K. This temperature assumption is a source of uncertainty in our estimated values of L_X. Recent work (Acton, Weston, & Bruner 1998) has shown that assuming $T = 3 \times 10^6$ K results in errors of up to factor of 2 in L_X for several different active region differential emission measure distributions, if the wavelength range includes the 2.8–37.1 Å spectral range coinciding with the SXT thin aluminum filter bandpass. We found only a slight increase between the estimated luminosity from 1 to 300 Å versus that from 2.8 to 37.1 Å . We therefore anticipate that our values of L_X are accurate to a factor of 2.

3. ANALYSIS OF THE DATA

The data set resulting from the above procedure consists of 333 data points with values of X-ray luminosity L_X and the global magnetic quantities Φ_{tot}, $B_{z,tot}^2$, J_{tot}, $B_{\perp,tot}^2$, and α_{ls}. Our primary goal is to characterize the relationship of L_X with the measured magnetic quantities. Figure 2 shows scatter plots of L_X versus various global magnetic quan-

tities; Figures 3 and 4 show some of the relationships between different magnetic variables.

Before discussing the relationship between L_X and the magnetic variables, it is useful to comment on some important relationships between some of the magnetic variables. Figure 4a shows that the auxiliary variable $\bar{A}$, which can be thought of as the effective magnetic area of the active region, is extremely well correlated and almost linear with the magnetic flux (we find $\bar{A} \sim \Phi_{tot}^{0.82}$), while Figure 4b shows that the auxiliary variable $\bar{B}$, which is a characteristic field strength of the active region, is less well correlated with Φ_{tot} and increases only modestly ($\bar{B} \sim \Phi_{tot}^{0.18}$). Thus, the range of magnetic fluxes in our data set reflects primarily the variation in the physical size of the active regions, rather than in their field strength. Figures 4c and 4d explore the variation of $B_{\perp,tot}^2/B_{z,tot}^2$ and $\mu_0 J_{tot}/\Phi_{tot}$ with magnetic flux. Evidently, the ratio of horizontal to vertical magnetic energy density increases just slightly with active region size, while the ratio of unsigned current to unsigned flux decreases significantly with the size of the active region. This latter trend is reminiscent of the "Σ effect" (Longcope, Fisher, & Pevtsov 1998), in which large-scale currents in active regions result from twists imparted to active region magnetic flux tubes by convective motions during the process of emergence through the convection zone. The amount of twist introduced by the Σ effect is predicted to vary as $\Phi_{tot}^{-0.7}$, qualitatively similar to what we see here ($\mu_0 J_{tot}/\Phi_{tot} \sim \Phi_{tot}^{-0.54}$).

Figure 2 shows that there is a clear relationship between the X-ray luminosity and each of the variables Φ_{tot}, $B_{z,tot}^2$, $B_{\perp,tot}^2$, and J_{tot}, indicating that L_X is highly correlated with some aspect of the active region magnetic field. However, it is not obvious from Figure 2 whether any of the displayed correlations result from a fundamental dependence of L_X on
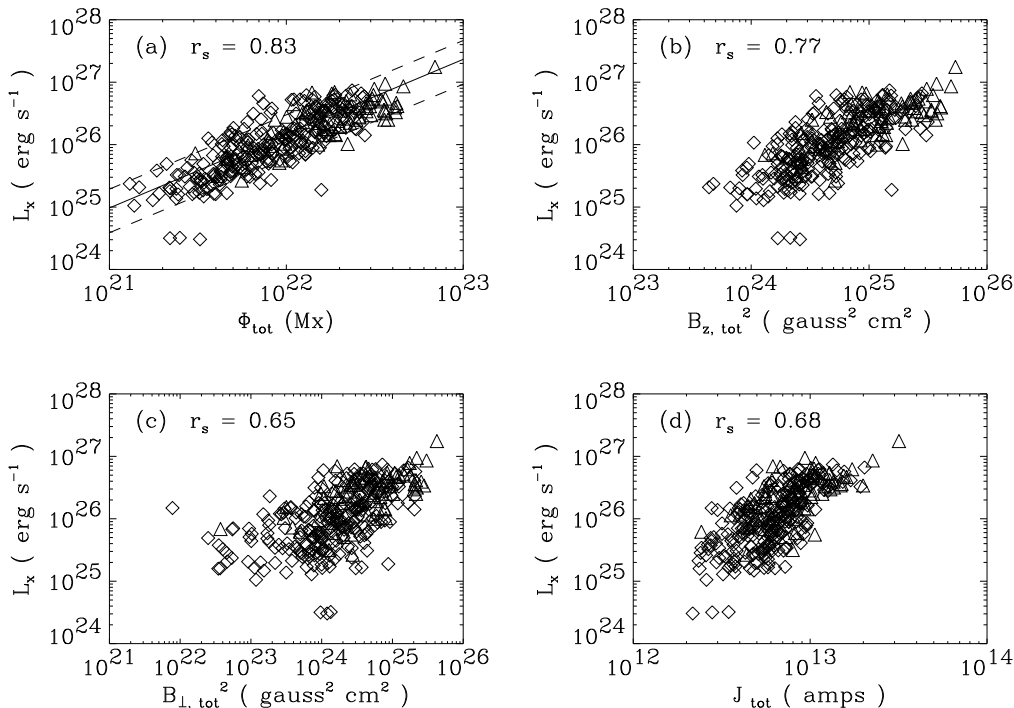

FIG. 2.—Scatter plots of X-ray luminosity versus the four global magnetic quantities Φ_{tot}, $B_{z,tot}^2$, $B_{\perp,tot}^2$, and J_{tot}. The Spearman correlation coefficients for these cases are listed with each panel. The power-law relationship $L_X \sim \Phi_{tot}^{1.19}$ is shown (*solid line*) along with a band encompassing 80% of the data points (*dashed lines*). Triangles denote undersampled magnetograms, and diamonds denote critically sampled magnetograms.
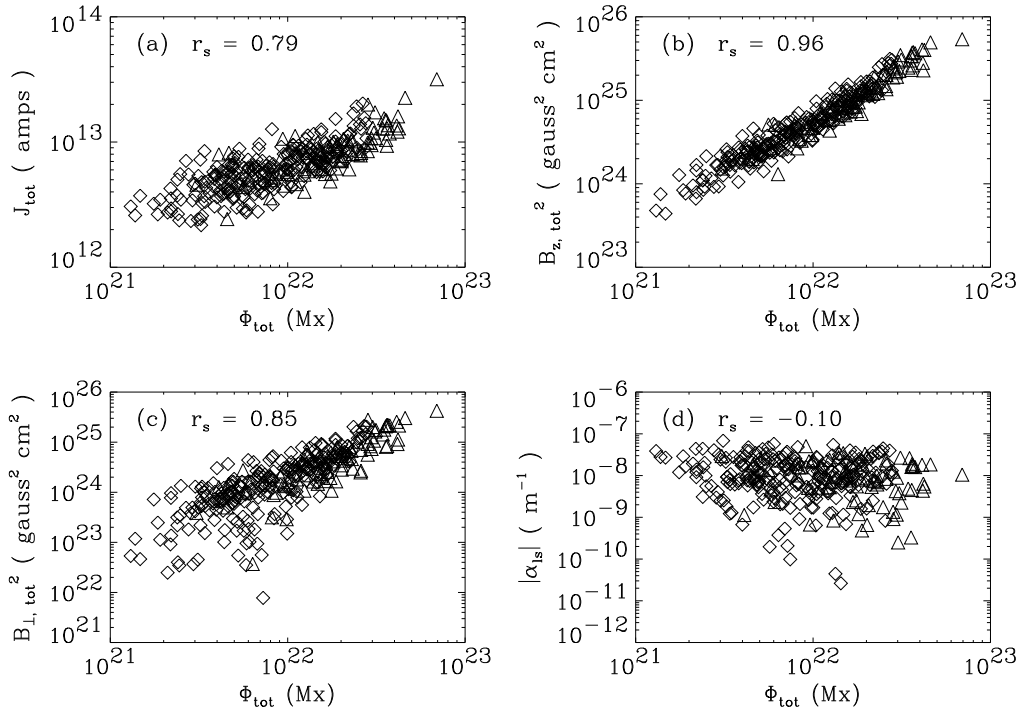
Fig. 3.—Scatter plots of global magnetic variables J_{tot}, $B^2_{z,tot}$, $B^2_{\perp,tot}$, and $|\alpha_{ls}|$ vs. Φ_{tot}. The Spearman correlation coefficients for each case are listed with each panel. Triangles denote undersampled magnetograms, and diamonds denote critically sampled magnetograms.

these global variables or whether the relationship is between L_X and some other "hidden" magnetic variable. The situation is muddied by the fact that these four extrinsic magnetic variables are all highly correlated with each other (Fig. 3), reflecting the fact that a large active region tends to have more of everything than does a smaller one. A general

feature of Figures 2 and 3 is that in logarithmic coordinates, the data points seem to scatter about lines, suggesting power-law relationships between the magnetic variables themselves and between the magnetic variables and L_X.

In contrast to the strong relationship between L_X and the global variables described above, there is little if any corre-
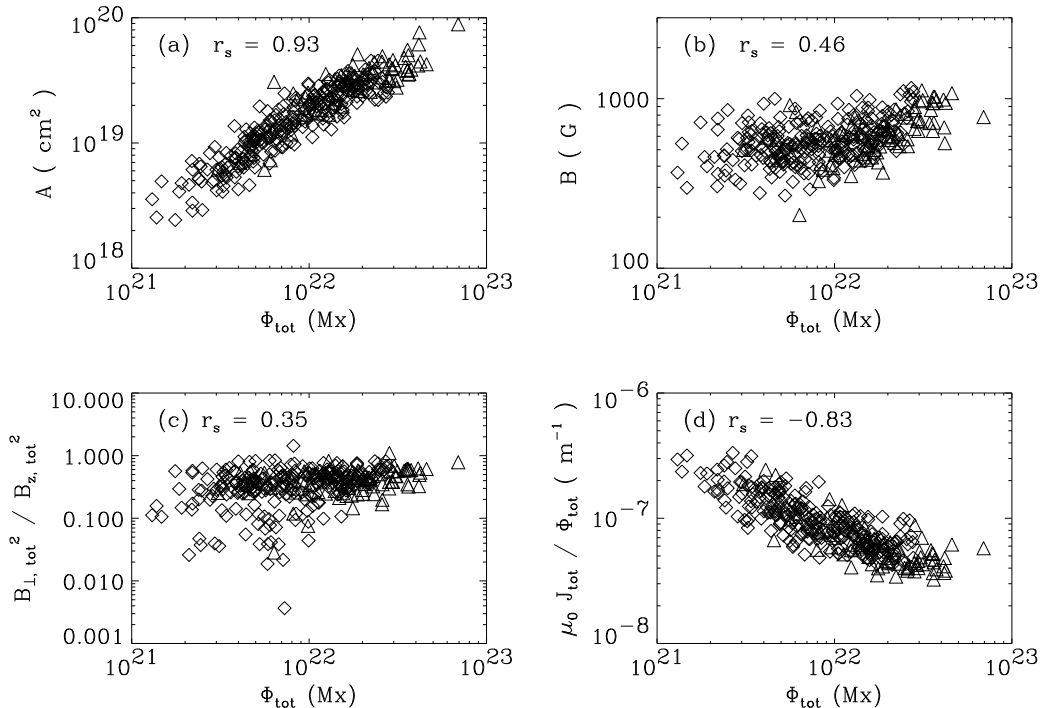

Fig. 4.—Scatter plots of the magnetic variables $\bar{A}$, $\bar{B}$, $B^2_{\perp,tot}/B^2_{z,tot}$, and $\mu_0 J_{tot}/\Phi_{tot}$ vs. Φ_{tot}. The value of $B^2_{\perp,tot}/B^2_{z,tot}$ averaged over the sample of active regions is 0.39. Triangles denote undersampled magnetograms, and diamonds denote critically sampled magnetograms.
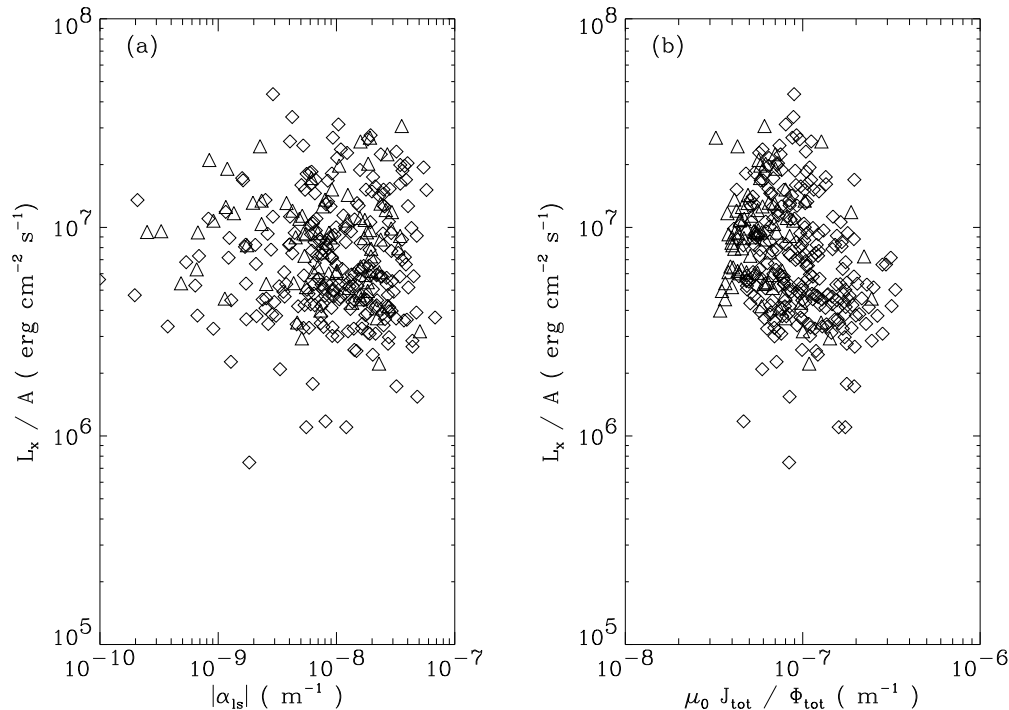
Fig. 5.—Scatter plots of $L_X/\bar{A}$ vs. $|\alpha_{ls}|$ and $\mu_0 J_{tot}/\Phi_{tot}$. Triangles denote undersampled magnetograms, and diamonds denote critically sampled magnetograms.

lation between either L_X or $L_X/\bar{A}$ and α_{ls}, leading us to conclude that α_{ls} has little to do with coronal heating. In Figure 5, we show the relationship between $L_X/\bar{A}$ (the X-ray luminosity divided by the effective magnetic area, a quantity similar to the X-ray surface flux) and α_{ls}, as well as that between $L_X/\bar{A}$ and $\mu_0 J_{tot}/\Phi_{tot}$, a quantity that has the same units as α_{ls}.

To help disentangle the relationship between the magnetic variables and L_X, we perform a *principal component analysis* (Kendall, Stuart, & Ord 1983) on the logarithms of L_X, Φ_{tot}, $B^2_{z,tot}$, $B^2_{\perp,tot}$, and J_{tot}. We have used logarithms because of the power-law behavior suggested by the scatter plots (a similar analysis of logarithmic variables is that of Majer et al. 1986, who studied the dependence of X-ray luminosity in RS CVn systems with rotation period and stellar spectral type). We have omitted α_{ls} from the principal component analysis since it is clear from the outset that there is no strong connection between L_X and this variable.

The mean of each sample of the logarithmic variables is subtracted from its corresponding distribution, and each variable is then rescaled to unit variance. The covariance matrix is constructed for the five rescaled variables; the off-diagonal elements of this symmetric matrix are in fact just the linear (Pearson) correlation coefficients between each combination of the five variables. The eigenvalues and eigenvectors of the covariance matrix are found and ordered from the largest to smallest eigenvalue. The ratio of the largest eigenvalue to the sum of eigenvalues reflects the fraction of total variation in the data set that is accounted for by the corresponding eigenvector, which in turn describes the combination of measured variables that "varies" most over the data.

For our five variables, the largest eigenvalue accounts for 83.1% of all variance within the data set, with the next largest eigenvalues accounting for 8.7% and 5.4%, respec-

tively. From a practical standpoint, this means that almost all of the variation in log L_X can be accounted for by correlation with a single logarithmic magnetic variable or a single linear combination of logarithmic magnetic variables. For the combination of magnetic variables defined by the eigenvector, the correlation coefficient with log L_X has the value 0.831. The correlation of log L_X with log Φ_{tot} has essentially the same value (0.829) and is much stronger than correlations of L_X with J_{tot} (0.68), with $B^2_{z,tot}$ (0.75), and with $B^2_{\perp,tot}$ (0.60). After exhaustive tests with many different combinations of magnetic variables, we found no other magnetic variable or combination of variables that is significantly better correlated to L_X than Φ_{tot} (although the correlation of L_X with $\bar{A}$ [0.826] is almost as good). This suggests that log L_X is primarily a function of log Φ_{tot}, with other magnetic variables playing a minor role. The conclusion that L_X is primarily related to Φ_{tot} is also reached through a completely different analysis using a nonparametric fitting technique (see, e.g., Porter & Klimchuk 1995).

To test a possible relationship between flux Φ_{tot} and L_X one must first find the "best" power law relating Φ_{tot} and L_X. This is done by computing the Spearman correlation coefficient r_s between Φ_{tot} and the quantity $\lambda_\Phi \equiv L_X/(\Phi_{tot})^p$ for various powers p.[2] The power p is varied until the correlation vanishes ($r_s = 0$). We then have two variables Φ_{tot} and λ_Φ, which are completely uncorrelated with one another. As a result, the luminosity of each active region can be

---

[2] Nonparametric statistics, such as the Spearman rank-order coefficient r_s are frequently used in situations where distributions may differ from Gaussian, making more traditional linear statistics, such as the Pearson correlation coefficient, invalid (Press et al. 1986). Empirically, we find, however, that for all of the quantities discussed in this paper the Pearson correlation coefficient is numerically very close to the Spearman coefficient.

expressed as the product of the uncorrelated variables

$$L_{\rm X} = \lambda_\Phi \, \Phi_{\rm tot}^p \, . \qquad (10)$$

The full data set (333 points) yields a power-law index $p = 1.190 \pm 0.04$, where the error estimates are found from Monte Carlo resampling of the original data set using the bootstrap technique (see, e.g., Efron & Tibshirani 1991). Plotted against $\Phi_{\rm tot}$ (Fig. 6), λ_Φ does appear uncorrelated. The central 80% of the data points fall inside the range

$$6 \times 10^{25} \ {\rm ergs \ s^{-1}} < \lambda_\Phi < 3 \times 10^{26} \ {\rm ergs \ s^{-1}} \, , \qquad (11)$$

where in the definition of λ_Φ we have normalized $\Phi_{\rm tot}$ to units of 10^{22} Mx. The mean and median values of λ_Φ are 1.5×10^{26} and 1.2×10^{26} ergs s^{-1} respectively.

The variable λ_Φ is the X-ray luminosity of an active region corrected for the flux dependence we have found. Thus, active regions with identical magnetic fluxes can exhibit different X-ray luminosities that are then reflected in differing values of λ_Φ. If other magnetic variables are important, there should be a dependence of λ_Φ on them that we can test. In particular, Spearman correlation coefficients r_s can be computed between λ_Φ and all other magnetic variables to search for additional dependencies. A natural candidate would be $J_{\rm tot}$, since active regions with more nonpotential magnetic energy (and hence currents), might be heated more effectively. Remarkably, λ_Φ and $J_{\rm tot}$ show no evidence of being correlated: Their Spearman coefficient is $r_s = 0.03$, which is consistent with 333 pairs of uncorrelated values at a high confidence level. Taken by themselves $L_{\rm X}$ and $J_{\rm tot}$ are highly correlated ($r_s = 0.68$), but the behavior of λ_Φ suggests that this correlation is a by-product of each variable's independent correlation to $\Phi_{\rm tot}$. Most importantly, this argues strongly that the luminosity variation reflected in λ_Φ is *not* related to the current $J_{\rm tot}$.

Other variables that show little or no correlation with λ_Φ include $B^2_{z, {\rm tot}}$ ($r_s = -0.07$), $B^2_{\perp, {\rm tot}}$ ($r_s = -.11$), α_{ls} ($r_s = 0.06$), $J_{\rm tot}/\Phi_{\rm tot}$ ($r_s = 0.04$), unsigned heliographic latitude ($r_s = 0.01$), and date of observation ($r_s = -0.05$). The only variable we have found that is significantly (anti-) correlated with λ_Φ is the derived variable $\bar B = B^2_{z, {\rm tot}}/\Phi_{\rm tot}$, with a Spearman coefficient $r_s = -0.28$. However, a scatter plot between λ_Φ and $\bar B$ shows that while the anticorrelation can be discerned, it is not a strong effect in comparison with the overall level of scatter. We speculate that a weak anticorrelation might result from the empirical fact that regions of strong magnetic field, such as sunspot umbrae, are typically darker in X-rays than regions of intermediate field strength such as plage.

Since the two magnetic quantities $\Phi_{\rm tot}$ and $J_{\rm tot}$ are themselves strongly correlated ($r_s = 0.79$) one might think that their roles could be reversed in the above process, but such is not the case. The quantity $\lambda_J \equiv L_{\rm X}/(J_{\rm tot})^q$ is independent of $J_{\rm tot}$ for the power-law index $q = 1.68 \pm 0.07$. However, λ_J is significantly correlated with $\Phi_{\rm tot}$ ($r_s = 0.38$) and remains so for a range of power-law index q well outside its error bars. Similar results are obtained for correlations of λ_J and $B^2_{z, {\rm tot}}$. The asymmetry in the behavior of λ_J versus that of λ_Φ suggests that the flux $\Phi_{\rm tot}$ plays a more fundamental role in determining $L_{\rm X}$ than does the current $J_{\rm tot}$ and reinforces the idea that $L_{\rm X}$ and $J_{\rm tot}$ are correlated only through their mutual correlations with $\Phi_{\rm tot}$. Examination of quantities $\lambda_{B_{z, {\rm tot}^2}}$ and $\lambda_{B_{\perp, {\rm tot}^2}}$ leads to similarly significant correlations with the other magnetic variables and strengthens our conclusion that the fundamental relationship is between $L_{\rm X}$ and $\Phi_{\rm tot}$.

How robust is the power-law value relating $L_{\rm X}$ to $\Phi_{\rm tot}$? Could the value $p = 1.19 \pm 0.04$ be an artifact of the nonparametric fitting technique we have used? To investigate this, we have also performed least-squares fits of log $L_{\rm X}$ to
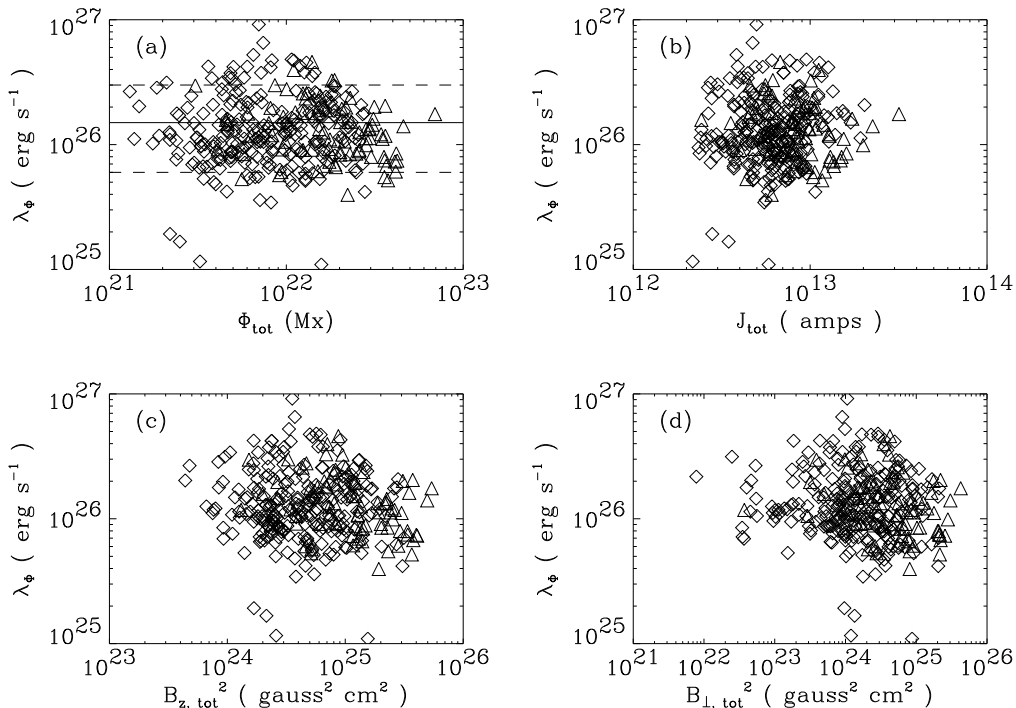

FIG. 6.—Quotient λ_Φ plotted against the global magnetic quantities $\Phi_{\rm tot}$, $J_{\rm tot}$, $B^2_{z, {\rm tot}}$, and $B^2_{\perp, {\rm tot}}$. Horizontal lines in top left-hand panel show the median value (*solid line*) and values encompassing the central 80% (*dashed lines*) of the data. Triangles denote undersampled magnetograms, diamonds denote critically sampled magnetograms.

log Φ_{tot} and found the same value of p to within 1%. Another concern is whether the undersampled (81 magnetograms) and critically sampled (252 magnetograms) subsets of the data display substantially different behavior. Performing the nonparametric treatment on the critically sampled and undersampled subsets of the data separately yields power laws $p = 1.25 \pm 0.06$ and $p = 1.00 \pm 0.09$, respectively, with very similar values found from least-squares fits. Thus, there does seem to be some modest systematic difference between the two subsets, but it is not clear whether this reflects the preponderance of large active regions seen during the early part of the *Yohkoh* mission (when most of the undersampled data was taken) or is an effect of the different rastering algorithm in the two data sets discussed in § 2.1. It is possible, for example, that the smaller power-law index for the undersampled case might be an effect of a magnetic filling factor, which itself depends on the amount of active region flux.

4. DISCUSSION

To summarize the results of § 3, we find that the best predictor of an active region's X-ray luminosity is simply its total unsigned magnetic flux Φ_{tot}. While other magnetic variables also correlate well with L_X, these correlations can be ascribed entirely to the correlation of those variables with Φ_{tot}. The dependence of L_X on Φ_{tot} evidently does not result from a dependence of L_X on J_{tot}, $B_{z,tot}^2$, or $B_{\perp,tot}^2$, and we find no significant residual correlation between L_X and the other variables once the dependence of L_X on Φ_{tot} has been accounted for.

How do these results compare with other recent work? A detailed study of NOAA AR 6952 (Metcalf et al. 1994) showed that there was little if any correlation of the locations of bright X-ray loops with any magnetic quantity, although the brightest emission occurred near the magnetic neutral line. On the other hand, other recent work (Falconer et al. 1997) compared the detailed spatial distribution of X-ray emission in five active regions observed by *Yohkoh* with magnetic field measurements from the NASA Marshall Space Flight Center vector magnetograph. They also find that the brightest emission occurs adjacent to magnetic neutral lines. Additionally, they found that most of the bright features have a footpoint rooted near strong-shear neutral lines (i.e., large-scale currents are present). A subsequent study of the total X-ray luminosity (Falconer 1997), similar to the one we have done, finds that over a small sample size, L_X is best correlated with the length of the sheared neutral line.

This latter conclusion could be viewed as contradicting our findings, since sheared neutral lines are believed to result from field-aligned currents. (R. L. Moore 1996, private communication) has suggested that correlation with current should be most pronounced in larger active regions and was therefore more evident in the study of Falconer (1997) than in our large data set. To test this possibility with our data, we have divided the data into two subsets, the first consisting of the 66 largest active regions (i.e., the largest 20%), the other consisting of the remaining 267. λ_{Φ} can again be plotted as a function of J_{tot}, using different symbols for the two different subsets (see Fig. 7). Figure 7 shows that there is a systematic difference in J_{tot} between the largest active regions and the rest of the sample: large regions have bigger currents. However, Figure 7 shows no obvious correlation of λ_{Φ} with J_{tot} when considering only the
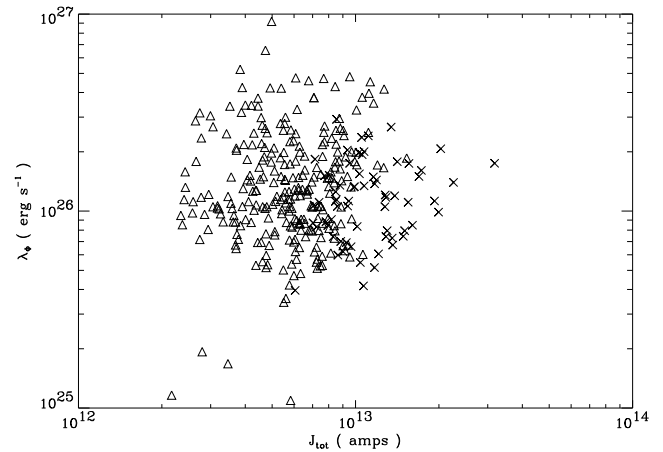

FIG. 7.—Scatter plot of λ_{Φ} vs. J_{tot}, showing the largest (in magnetic flux) 20% of active regions as crosses and the remaining active regions as triangles.

largest active regions; further, the range of λ_{Φ} is not significantly different than that for the entire sample. This implies that if shearing along neutral lines does affect the X-ray luminosity globally, its connection to the global current variable J_{tot} is too subtle to be detected as a correlation between λ_{Φ} and J_{tot} in our data set.

4.1. Constraints on Heating Models

Our measured relationship between L_X and Φ_{tot} (and the relationships with the other global magnetic variables) can be used to test or constrain several existing models for coronal heating.

4.1.1. Alfvén Wave Heating

Wave heating models have a Poynting flux given by equation (2) assuming that all wave energy is absorbed in the corona. For constant wave amplitude $\langle v^2 \rangle$, the total power dissipated in an active region is

$$P_{tot} = \sqrt{\frac{\rho}{4\pi}} \langle v^2 \rangle \Phi_{tot} . \qquad (12)$$

Taking the X-ray luminosity L_X to be a fraction f of this power and equating the coefficient of Φ_{tot} with the median value $\lambda_{\Phi} \simeq 1.2 \times 10^{26}$ ergs s^{-1} yields a wave amplitude

$$\langle v^2 \rangle_{phot}^{1/2} \simeq \frac{0.1\sqrt{Q}}{\sqrt{f}} \left(\frac{\Phi_{tot}}{10^{22} \text{ Mx}} \right)^{0.1} \text{ km s}^{-1} , \qquad (13)$$

at the photosphere where the flux is measured, assuming a mass density of $\rho = 1.0 \times 10^{-7}$ g cm^{-3}. Note that if Alfvén wave energy is absorbed less than perfectly, with a quality factor Q, the required wave velocity scales up by $Q^{1/2}$. At the photosphere, the required wave velocities are plausible, provided Q is not too great.

The model is put to a more stringent test at transition region temperatures. The required velocities can be scaled to expected transition region values by noting that Φ_{tot} should be the same at photospheric and transition region levels if most of the photospheric flux emerges to coronal heights and using an estimated transition region mass density of $\rho = 1.0 \times 10^{-15}$ g cm^{-3} (corresponding to a gas pressure of ~ 1 dyne cm^{-2} at a temperature of 10^5 K). We

then find

$$\langle v^2 \rangle_{t.r.}^{1/2} \simeq \frac{10\sqrt{Q}}{\sqrt{f}} \left(\frac{\Phi_{tot}}{10^{22} \ \text{Mx}} \right)^{0.1} \ \text{km s}^{-1} \ . \qquad (14)$$

Estimates of the quality factor Q can be found (McKenzie & Mullan 1997) by performing time series analyses of the brightness in active region coronal loops seen with the SXT telescope on *Yohkoh*. Periodic brightness modulation is observed with lower limits on Q ranging from 10 to 100 (see Table II of McKenzie & Mullan 1997). The brightness modulation is interpreted as evidence for global Alfvén resonances in loops. $Q = 10$ would yield ~ 30 km s^{-1} wave velocities, if f were unity. While similar values of $\langle v^2 \rangle_{t.r.}^{1/2}$ have been measured (Cheng, Doschek, & Feldman 1979; Dere & Mason 1993; Warren et al. 1997), the higher values of Q yield wave velocities that are too large. We conclude that a self-consistent picture incorporating our measured X-ray luminosities, velocities determined by transition region line broadening, and measured Q-values (McKenzie & Mullan 1997) is not possible in the context of the Alfvén wave heating model.

In summary, the wave heating model does predict that L_X should be most strongly related to Φ_{tot}, as is observed, but there seems to be insufficient energy in the waves observed at transition region temperatures to account for the observed level of heating.

4.1.2. *Nanoflare Heating*

One can use a similar comparison to examine stress heating models, whose Poynting flux is given by equation (3) and leads to a net power scaling as

$$P_{tot} \sim |v| B_{z,tot}^2 \ . \qquad (15)$$

This suggests that such models would exhibit the strongest correlation between L_X and $B_{z,tot}^2$. In our data, this correlation was not as significant as that between L_X and Φ_{tot} (see § 3). It is nevertheless possible to compare the predictions of one specific version of this model, Parker's nanoflare hypothesis (Parker 1988), and our observed relationship between L_X and $B_{z,tot}^2$ to derive parameters of that model and then compare them with the values proposed (Parker 1988).

In Parker's nanoflare model, the energy for coronal heating comes from the intermittent dissipation of energy in small-scale coronal current sheets formed from the random shuffling of footpoint motions. The average power dissipated per unit surface area, W, is proposed to vary as

$$W \simeq B_z^2/4\pi \times v^2 t/L = B_z^2/4\pi \times v \tan \theta_{crit} \ , \qquad (16)$$

where L is the coronal loop length, v is the velocity of photospheric footpoint motion, and t is the time necessary to deflect the field direction sufficiently for the small-scale tangled field to be inclined from the large-scale field direction at some maximum critical angle $\tan \theta_{crit} = vt/L$. Parker proposes a value $\theta_{crit} \simeq 14°$ corresponding to $t \simeq 5 \times 10^4$ s for an assumed granulation velocity $v \simeq 0.5$ km s^{-1}, an assumed loop length of 10^9 cm, and an assumed $B_z \simeq 100$ G. The values of θ_{crit} and t were derived to match the estimated energy flux of 10^7 ergs cm^{-2} s^{-1} (Withbroe & Noyes 1977).

The left-hand side of equation (16) can be integrated over the active region and written as L_X/f, where f is the fraction of the total dissipated power appearing in the form of

X-rays. Equating this to the area integral of the right-hand side, we find

$$L_X \simeq fv \tan \theta_{crit} B_{z,tot}^2/4\pi \ . \qquad (17)$$

The data can then be used to derive the coefficient $fv \tan \theta_{crit}/4\pi$. If the relationship between L_X and $B_{z,tot}^2$ is assumed to be linear [which is not quite correct—a least-squares fit results in $L_X \sim (B_{z,tot}^2)^{0.87}$], then an average value of $L_X/B_{z,tot}^2$ from the entire data set yields $fv \tan \theta_{crit} \simeq 360$ cm s^{-1}. This value of $v \tan \theta_{crit}$ is about 1.5 orders of magnitude smaller than the value proposed (Parker 1988). The discrepancy between the value we derive from the data and Parker's number can be accounted for by the difference between the field strength he assumed (100 G) and the much larger field strengths in the data (averaged over all the active regions, we find $\bar{B} \simeq 600$ G). For Parker's assumed value of $v \simeq 0.5$ km s^{-1}, this results in $\theta_{crit} \simeq 0°.4/f$, as compared with 14°. Alternatively, if $\theta_{crit} \simeq 14°$, then the required footpoint shuffling velocity is $v \simeq 0.014$ km s$^{-1}/f$.

In summary, the nanoflare model (Parker 1988) overestimates the amount of energy radiated in our active region data by about 1.5 orders of magnitude. That problem could be easily resolved by adjusting either the critical angle or the footpoint shuffling velocity in the model downward. The remaining problem with the nanoflare model is that it predicts the strongest relationship to be between L_X and $B_{z,tot}^2$, rather than being between L_X and Φ_{tot}, as the data seem to show.

4.1.3. *Heating from the MCC Model*

There is a recently published stress heating model that predicts a relationship between L_X and the global magnetic variables that is more consistent with the observations. This model, the "Minimum Current Corona" (MCC), describes coronal heating as a series of small reconnection episodes punctuating the quasi-static evolution of the coronal field (Longcope 1996; Longcope & Cowley 1996). These reconnection events occur at topologically significant field lines called "separators." Prior to reconnection, motion of the photospheric flux causes the development of intense current ribbons along the separators. This current stores magnetic energy, which is ultimately liberated by reconnection. An estimate of the heating power in this model is the product of the amplitude and frequency of reconnection events (Longcope 1996) rather than being given as a Poynting flux.

Unfortunately, current work on the minimum current corona has yet to yield a quantitative heating rate. Nevertheless, its general properties indicate a scaling law that applies under several assumptions, described in the Appendix. For an average velocity of photospheric flux elements $\bar{v}$ and active region area A the scaling law is

$$P_{tot} \sim \bar{v} \Phi_{tot}^2 / A \qquad (18)$$

(see Appendix). The linearity in velocity is analogous to the same dependence in a mechanical friction (Longcope 1996; Longcope & Cowley 1996). Using $\bar{A}$ as an estimate of the active region area, which we find scales as $\bar{A} \sim \Phi_{tot}^{0.819}$ in our data, leads to a predicted scaling

$$L_X \sim f\bar{v} \Phi_{tot}^{1.18} \ , \qquad (19)$$

where, as before, f represents the fraction of the total power P_{tot} that is emitted in X-rays. While this power law is very

close to our derived power-law relationship between L_X and Φ_{tot}, there are undoubtedly systematic variations of f with active region size and/or temperature, owing to the insensitivity of the SXT bandpass to lower temperature coronal plasma. We therefore caution that the agreement in power-law index between the data and this theoretical model might not be this good if these effects were accounted for properly. The main point is that this coronal heating picture predicts an active region luminosity that depends mainly on the total magnetic flux, similar to what we find.

The MCC model also predicts qualitatively how emission should be distributed within the active region. Equation (A2) from the Appendix illustrates that flux elements separated by only short distances, such as those just across the neutral line from one another, will have correspondingly short separator loops, and the total power dissipated by these elements will scale roughly as l^{-2}, where l is the characteristic separation scale length between magnetic poles. This means that the dissipation of power will tend to be concentrated near the neutral line (Metcalf et al. 1994; Falconer et al. 1997), as we found empirically when comparing the magnetograms with the SFD images. Because the greater dissipation in loops close to the neutral line is also concentrated into smaller, lower lying coronal volumes, the surface brightness distribution of the X-ray emission should appear to be especially concentrated near the neutral line.

If the MCC model really describes how coronal heating takes place, can one use the currents derived from vector magnetographs (such as the HSP) to derive meaningful measurements of the currents driving coronal heating? The answer to this is not clear. The distribution of currents in the MCC model is extremely nonuniform; the current density is essentially zero except along the magnetic separa-

tor loops, where it is highly concentrated into thin ribbons. It is not obvious whether these concentrated structures would contribute meaningfully to the large-scale current as measured by a vector magnetograph. Since the current ribbons form in the corona and close along the photosphere in the theoretical model, it is also not clear whether such currents would be measurable at those depths in the atmosphere where the magnetic field is measured.

4.1.4. Comments on Active Region Energetics

The previous subsections showed that Alfvén waves contributed insufficient energy to explain the X-ray data and that the nanoflare model, at least with the parameters described by Parker (1988), contributed too much energy. The MCC model is not sufficiently well developed to predict a specific energy dissipation rate, so that its energetic predictions remain untested. In the context of these models, it is useful to point out some interesting features of active region energetics that one finds in the data.

The vector magnetograms allow for an estimate of the total magnetic energy E_{mag} by using the B_z field to extrapolate a potential field configuration above the photosphere (e.g., Gary 1989). The true chromospheric and coronal magnetic energy is observed to be as much as 50% greater than the potential field energy (Metcalf et al. 1995), but for our needs the potential field energy is a reasonable estimate. Figure 8b shows that the potential field energy E_{mag} is highly correlated with Φ_{tot} and that the range of magnetic energies of our sample of active regions is between $\sim 10^{31}$ and $\sim 3 \times 10^{33}$ ergs. A least-squares fit yields $E_{mag} \sim \Phi_{tot}^{1.35}$. Figure 8c shows the behavior of L_X as a function of E_{mag}, from which it can be seen that L_X is an increasing function of E_{mag} (a least-squares fit yields $L_X \sim E_{mag}^{0.75}$). The ratio
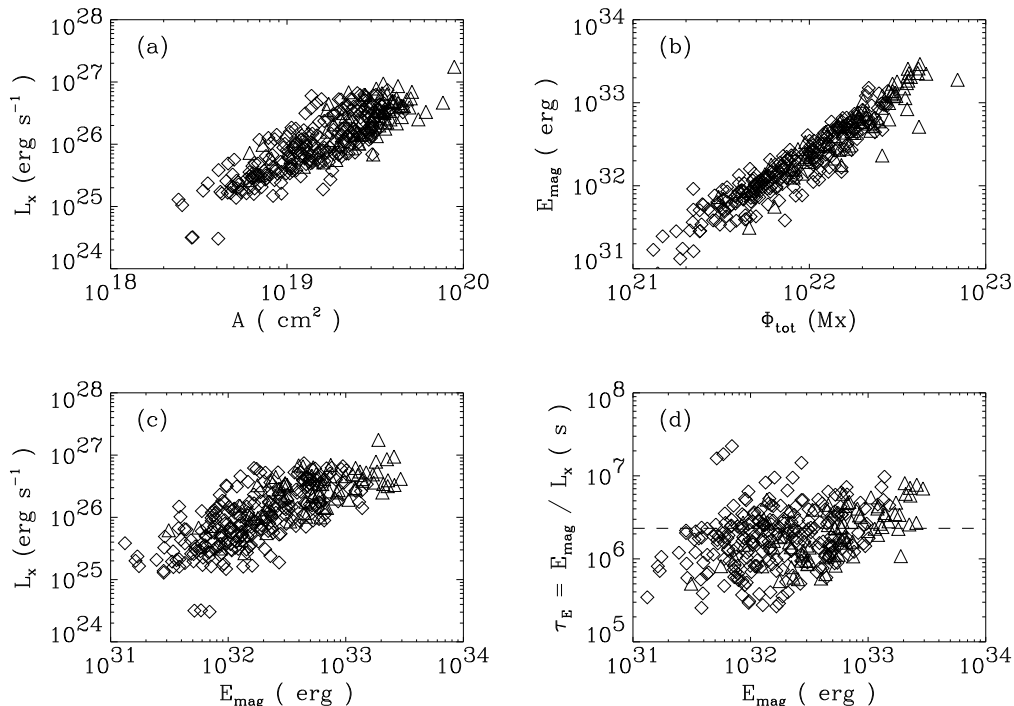

FIG. 8.—X-ray luminosity L_X as a function of $\bar{A}$ (a). Potential field magnetic energy E_{mag} as a function of Φ_{tot} (b). L_X as a function of E_{mag} (c). Timescale $\tau_E \equiv E_{mag}/L_X$ (d). Dashed line indicates a solar rotation time of 27 days. Diamonds indicate critically sampled magnetograms, and triangles denote undersampled magnetograms.

$E_{\mathrm{mag}}/L_X \equiv \tau_E$ yields a characteristic timescale, which is plotted as a function of E_{mag} in panel d of Figure 8, with the dashed line indicating a period of 27 days (1 solar rotation period) for comparison. From Figure 8, it is clear that τ_E is typically a solar rotation period (but with considerable scatter). The values of τ_E are not drastically different from the observed lifetime of active regions. Whether or not τ_E has any causal connection to the lifetime of active regions, the relationship between L_X and E_{mag} provides an interesting constraint on coronal heating mechanisms and one that is not addressed by any of the theories discussed here.

5. CONCLUSIONS

Much can be learned about the nature of coronal heating by using statistical studies of global magnetic properties of a diverse set of active regions. Our analysis of the data suggests that the best magnetic indicator of the X-ray luminosity of an active region is simply its total unsigned magnetic flux and that large-scale currents, at least as measured by J_{tot}, do not appear to affect the X-ray output. We have discussed this result within the context of several different heating models. We find that while the Alfvén wave heating model correctly predicts that the magnetic variable best correlated with L_X is Φ_{tot}, the observed level of heating is too great to be consistent with measured transition region line widths and expected Q-values of the global resonances. The nanoflare model (Parker 1988) predicts a best relationship being between L_X with $B_{z,\mathrm{tot}}^2$, rather than between L_X and Φ_{tot}. In contrast to the wave heating model, there is ~ 36 times *more* heating energy available in the model than is seen in the data. The MCC model gives a scaling of L_X with Φ, which seems to be consistent with the observed power-law index $p = 1.19$, but the model is not sufficiently well developed to predict a numerical coefficient connecting the two quantities.

We have shown that the magnetic energy estimated from the vector magnetograms yields $E_{\mathrm{mag}} \sim \Phi_{\mathrm{tot}}^{1.35}$, with active region magnetic energies varying from $\sim 10^{31}$ to $\sim 3 \times 10^{33}$ ergs in our data. We have shown that the ratio of the magnetic energy to the X-ray luminosity leads to timescales of order 1 month. The observed relationship between L_X and E_{mag} provides an important constraint on coronal heating mechanisms.

It is interesting to place the active region data within the context of other active stars. In Figure 9, we compare values of L_X and Φ_{tot} from solar active regions with corresponding values of L_X and estimates of magnetic fluxes of nearby G, K, and M dwarf stars (Saar 1996). To convert magnetic field strengths and filling factors to magnetic fluxes, we have multiplied the filling factor and field strength by the estimated stellar surface area. X-ray luminosities are similarly converted from surface fluxes (Saar 1996) by multiplying by the stellar surface area. Note that there appears to be a horizontal offset between the stellar data and the solar active region data, but the overall slope of the two different data sets seems consistent. Given that the magnetic fields are measured in completely different ways (spatially resolved polarization measurements versus spectral line fitting), that the coronal temperatures of the active stars may be considerably hotter than the solar active regions, and that the X-ray measurements were made with different instruments, an offset is not surprising. The important point is that the power-law dependence between magnetic flux and
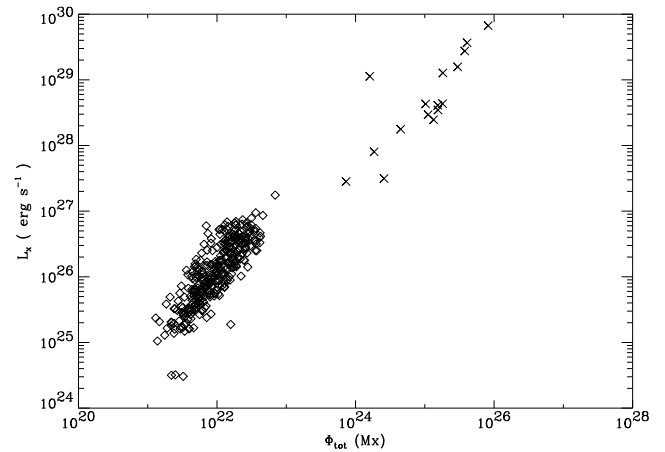

FIG. 9.—Plot of L_X vs. Φ_{tot} for the set of active regions in this paper (*diamonds*), as well as estimated magnetic fluxes and X-ray luminosities for nearby active G, K, and M dwarf stars (Saar 1996; *crosses*).

X-ray luminosity appears to be quite similar and therefore suggests a "universal" relationship between magnetic flux and the amount of coronal heating. It is also interesting that the power-law dependence we have found for solar active regions ($L_X \sim \Phi_{\mathrm{tot}}^{1.19}$) is similar (although not equal) to the power law found by Schrijver et al. 1989 ($p \simeq 0.90$) in their earlier comparison of X-ray fluxes and magnetic field measurements.

In the future, there are many improvements to be made, and further investigations of our data set that will be done. In particular, the magnetogram data can be reanalyzed to account not only for current-sensitive variables such as J_{tot}, but also the length of neutral lines and sheared neutral lines (Falconer 1997). Our large and diverse sample size will allow us to test more rigorously whether the length of sheared neutral lines is a predictor of coronal heating. If so, the morphology of the active regions can be investigated to see why this is not reflected in the sensitivity of L_X to J_{tot}.

Finally, our work suggests that further and more stringent observational tests of the MCC heating model (Longcope 1996) are necessary and that further work on development of the model is needed. A prediction of that work is that the brightest coronal emission should coincide spatially with the location of magnetic separator loops, which can be predicted directly from magnetogram data. Details of the coronal images, rather than just total luminosities, must be examined, but with the advent of the new generation of high-resolution solar coronal imaging instruments (e.g., EIT, TRACE) this is certainly possible. The model also needs to be developed to the point that a more quantitative comparison between its predictions for X-ray luminosity as a function of global magnetic quantities can be made with the data presented here.

The values of L_X and the global magnetic variables from this study can be obtained by contacting George H. Fisher.

APPENDIX A

APPENDIX: THE MCC HEATING MODEL

Longcope (1996) has developed a qualitatively new picture for how energy is stored and dissipated in the solar corona. In this model, the MCC, the coronal portion of an active region is described to a first approximation as the vacuum field resulting from a photospheric distribution of point magnetic charges, whose locations correspond to the tops of magnetic flux elements (flux tubes) piercing the photosphere (see also Demoulin, Henoux, & Mandrini 1994). In a bipolar active region, where the positive and negative fluxes essentially balance, the corresponding total positive and negative magnetic charges would also balance. The amplitude of each point charge is equal to the amount of flux in a given magnetic flux concentration. As the photospheric flux elements are moved around, either by convective motions or because of the dynamics of the underlying flux rope system, the evolving vacuum field configuration would necessarily imply changes in the amounts of magnetic flux connecting one magnetic element to another. If this were exactly true, however, the vacuum approximation would violate the frozen-in flux conditions believed to exist in the highly conducting corona. The motion of the magnetic charges (flux tubes) must therefore result in the formation of currents that maintain the frozen-in condition. It has been shown (Longcope 1996; Longcope & Cowley 1996) that the resulting currents flow in thin, closed ribbon-like "magnetic separator loops" connecting magnetic null points (where the field strength is zero). Continued motion of the magnetic charges builds up the current along these loops until the coronal plasma can no longer sustain the increased current density and the fields near the separator loop suddenly relax to the new vacuum field configuration corresponding to the new magnetic charge locations. This releases energy along the coronal loops immediately adjacent to the magnetic separator field lines.

In the MCC model (Longcope 1996), the average power dissipated by a single separator loop associated with a given magnetic charge Ψ_i within an active region, moving with speed v, is

$$P_i = \theta v \frac{I^*}{2c} \left| \frac{d\Psi^v}{dx} \right| , \tag{A1}$$

where I^* is the "characteristic" current that will flow in the separator loop associated with the motion of that magnetic charge, $d\Psi^v/dx$ is the rate of flux change of the vacuum field through the separator loop with respect to the motion of the given charge Ψ_i, and θ is a dimensionless threshold (generally assumed to be small compared with unity), which parameterizes how great the separator loop current can become before it is suddenly dissipated. One can determine from the model how this dissipation rate scales with the charge Ψ_i and the characteristic length scale l describing the typical distance between opposite magnetic charges in the active region. From Appendix B of Longcope (1996), $I^* \propto \Psi_i/l$ and $d\Psi^v/dx \propto \Psi_i/l$, meaning that

$$P_i \propto v\Psi_i^2/l^2 . \tag{A2}$$

The power dissipated by the entire active region will consist of a sum of contributions similar to that of equation (A1), with the possible complication of mutual inductance terms between multiple separator loops (see § 5 of Longcope 1996). It is nevertheless clear from equation (A2) that the power dissipated by the active region will in general be dominated by the motion of the largest magnetic flux concentrations Ψ_i. If we assume that active regions are "self-similar," that is, that the ratio of the largest flux concentrations to the total unsigned flux is roughly equal for large and small active regions, then we can use the total unsigned flux Φ_{tot} in an active region as a proxy for the largest charges Ψ_i in equation (A2). The self-similar approach can also be used to argue that the area A of the active region can serve as a proxy for the quantity l^2. Making these substitutions into equation (A2) and assuming that one sums over a similar number of the most important magnetic elements for both large and small active regions, results in

$$P_{tot} \propto \bar{v}\Phi_{tot}^2/A . \tag{A3}$$

REFERENCES

Acton, L. W. 1996, in Magnetodynamic Phenomena in the Solar Atmosphere: Prototypes of Stellar Magnetic Activity, ed. Y. Uchida, T. Kosugi, & H. Hudson (Dordrecht: Kluwer), 3
Acton, L. W., Weston, D. C., & Bruner, M. E. 1998, J. Geophys. Res.–Space Res.
Browning, P. K., Sakurai, T., & Priest, E. R. 1986, A&A, 158, 217
Canfield, R. C., et al. 1993, ApJ, 411, 362.
Cheng, C. C., Doschek, G. A., & Feldman, U. 1979, ApJ, 227, 1037
Delaboudiniere, J.-P., et al. 1995, Sol. Phys., 162, 291
Demoulin, P., Henoux, J. C., & Mandrini, C. 1994, A&A, 285 1023
Dere, K. P., & Mason, H. E. 1993, Sol. Phys., 144, 217
Edlen, B. 1937, Z. Phys., 104, 407
Efron, B., & Tibshirani, R. 1991, Science, 253, 390
Falconer, D. A. 1997, Sol. Phys., 176, 123
Falconer, D. A., Moore, R. L., Porter, J. G., Gary, G. A., & Shimizu, T. 1997, ApJ, 482, 519
Gary, G. A. 1989, ApJS, 69, 323
Golub, L., Maxson, C., Rosner, R., Serio, S., & Vaiana, G. S. ApJ, 1980, 238, 343
Grotrian, W. 1939, Naturwissenschaften, 27, 214
Hollweg, J. V. 1984, ApJ, 277, 392
Hudson, H. S. 1991, Sol. Phys., 133, 357

Kano, R., & Tsuneta, S. 1995, ApJ, 454, 934
Kendall, M., Stuart, A., & Ord, J. K. 1983, The Advanced Theory of Statistics, Vol. 3 (4th ed.; New York: MacMillan), 320
Klimchuk, J. A., & Canfield, R. C. 1994, in ASP Conf. Ser., 68, Solar Active Region Evolution: Comparing Models with Observations, ed. K. S. Balasubramaniam & G. W. Simon (San Francisco: ASP), 233
Klimchuk, J. A., Canfield, R. C., & Rhoads, J. R. 1992, ApJ, 385, 327
Longcope, D. W. 1996, Sol. Phys., 169, 91
Longcope, D. W., & Cowley, S. C. 1996, Phys. Plasmas 3(8), 2885
Longcope, D. W., Fisher, G. H., & Pevtsov, A. A. 1998, ApJ, 507, 417
Longcope, D. W., & Sudan, R. 1994, ApJ, 437, 491
Majer, P., Schmitt, J. H. M. M., Golub, L., Harnden, F. R. Jr., & Rosner, R. 1986, ApJ, 300, 360
McKenzie, D. E., & Mullan, D. J. 1997, Sol. Phys., 176, 127
Metcalf, T. R. 1994, Sol. Phys. 155, 235
Metcalf, T. R., Canfield, R. C., Hudson, H. S., Mickey, D. L., Wülser, J.-P., Martens, P. C. H., & Tsuneta, S. 1994, ApJ, 428, 860
Metcalf, T. R., Jiao, L., McClymont, A. N., Canfield, R. C., & Uitenbroek, H. 1995, ApJ, 439, 474
Mickey, D. L. 1985, Sol. Phys., 97, 223
Moore, R. L., Falconer, D. A., Porter, J. G., Gary, G. A., & Shimizu, T. 1996, BAAS, 188, 86.04

Parker, E. N. 1972, ApJ, 174, 499
———. 1983, ApJ, 264, 642
———. 1988, ApJ, 330, 474
———. 1996, ApJ, 471, 485
Pevtsov, A. A., Canfield, R. C., & Metcalf, T. R. 1994, ApJ, 425, L117
———. 1995, ApJ, 440, L109
Porter, L. J., & Klimchuk, J. A. 1995, ApJ, 454, 499
Press, W. H., Teukolsky, S. A., Vetterling, W. T., & Flannery, B. P. 1986, Numerical Recipes in Fortran: The Art of Scientific Computing, (2d ed.; Cambridge: Cambridge Univ. Press), 633

Saar, S. H. 1996, in Magnetodynamic Phenomena in the Solar Atmosphere: Prototypes of Stellar Magnetic Activity, ed. Y. Uchida, T. Kosugi, & H. Hudson (Dordrecht: Kluwer), 367
Schrijver, C. J., Cote, J., Zwaan, C., & Saar, S. H. 1989, ApJ, 337, 964
Skumanich, A., & Lites, B. W. 1987, ApJ, 322, 473
Tsuneta, S., et al. 1991, Sol. Phys., 136, 37
Warren, H. P., Mariska, J. T., Wilhelm, K., & Lemaire, P. 1997, ApJ, 484, L91
Withbroe, G. L., & Noyes, R. W. 1977, ARA&A, 15, 363